Multi-objective hull form optimization of a SWATH configuration using surrogate models

Paul Renaud, Matthieu Sacher, Yves-Marie Scolan

Version of Record: https://www.sciencedirect.com/science/article/pii/S0029801822006096
Manuscript_a5865410c7b0f5f5df8488119ba8d796

Multi-objective hull form optimization of a SWATH configuration using surrogate models

Paul Renaud[a,*], Matthieu Sacher[a], Yves-Marie Scolan[a]

[a]*ENSTA Bretagne, CNRS UMR 6027, IRDL, 2 rue Francois Verny, 29806 Brest Cedex 9, France*

Abstract

The present study introduces a surrogate-based multi-objective hull form optimization of a SWATH configuration, enabling optimal hull design compromises between seakeeping performance and ship resistance. A parametric model of a SWATH ship is built, which has variable horizontal torpedoes semi-axis and strut angle of inclination. The displacement is assumed to be constant and is balanced with the vertical semi-axis of torpedoes. The objective seakeeping function is the amplitude of vertical movement on the ship's gangway, calculated in irregular waves. As the energy dissipation of SWATH ships are mainly generated by viscous effects, these are estimated using empirical formulas and are added to the equations of motion. The ship resistance is computed with a finite volume solver using a RANS model. Three levels of fidelity, having increasing computation costs, are considered to model ship resistance. The first low fidelity level concerns the wetted surface of the hull. Due to their geometry, SWATH ships can be destabilized by the Munk moment and be dynamically unstable, which can lead to instabilities in resistance calculations. The medium-fidelity level then considers a free sinkage and a fixed pitch to ensure the stability of the calculations. The third higher-fidelity level considers stabilizing fins to counterbalance the destabilizing moment. Trim angles of fins are solved to reach moment equilibrium and the fins drag is included in the total ship resistance, which is to be minimized. The multi-objective optimization problem is solved for these three degrees of fidelity. Results differences between fidelity level approaches are also compared, in order to highlight the impact on the optimal hull designs of using a low-fidelity method, with regard to the computational costs.

Keywords: SWATH, multi-objective optimization, surrogate models, seakeeping, resistance

1. Introduction

Hull form optimizations have become popular since advances in computer technology have enabled complex physical problems to be assessed with great precision. To design more efficient vessels in term of power and energy saving, ship resistance optimization for conventional hull form has become essential in ship design (Cordier et al., 2011; Serani et al., 2016; Tahara et al., 2011). The movement of ships in waves is also critical, for reasons of safety, comfort, and operability. Multi-objective optimization studies (Diez et al., 2015) have demonstrated that it is possible to simultaneously increase several hydrodynamic performances. Unconventional hulls, such as Small Water Plane Area Twin-Hull configuration, were created specifically to reduce motions in waves and be operable in a harsh environment. Depending on the intended purpose of the ship, there are numerous geometrical otpions. The struts can be single or twin, inclined or not, and there are various torpedoes sections of existing ships. SWATH ships appear more efficient in terms of seakeeping than "standard" ships with the same displacement (Yun et al., 2019). The heave, roll and pitch resonance periods are long and the hull is deeply immersed which reduces the waves' radiation/diffraction forces. However, the wetted surface is generally more significant than that of a ship of the same size, which increases the skin friction resistance. This type of ship is outfitted with stabilizing fins that increase longitudinal stability impaired by the so-called "Munk moment" (Lee and Martin, 1976). The fins also provide damping during motion in waves.

*Corresponding author
Email address: paul.renaud@ensta-bretagne.org (Paul Renaud)

Optimization on SWATH configuration studies mainly focus on ship resistance. Reynolds-averaged Navier-Stokes (RANS) simulations can be used to estimate ship resistance. A Response Surface Model using a cubic polynomial interpolation is also integrated in (Lin et al., 2019) to predict ship resistance over the variability domain. The optimum design is finally found with the Multi-Island Genetic Algorithm. Multi-objective optimizations have been implemented with two cruising speeds in (Ni et al., 2020; Papandreou and Papanikolaou, 2015) where the ship resistance is evaluated using RANS simulations (Ni et al., 2020), or with analytical calculations using Michell's integral for the wave resistance, and the ITTC 57 formula for the viscous resistance (Papandreou and Papanikolaou, 2015). The optimal designs, which minimize resistance for both speeds, are identified by the Multi-Objective Particle Swarm Optimization algorithms in (Ni et al., 2020) and by the Non-Dominated Sorting Genetic Algorithm II (NSGA-II) in (Papandreou and Papanikolaou, 2015). Both algorithms build the Pareto Front (PF), representing the optimum balance of the two objective functions. The ship resistance is minimized while the displacement is simultaneously maximized in (Pellegrini et al., 2017). A multi-fidelity surrogate model has been implemented in (Pellegrini et al., 2017), reducing computational effort compared to a conventional optimization algorithm. The wave resistance is calculated by a potential code, the degree of fidelity depending on the mesh density, and viscous drag is estimated using the flat-plate approximation. In previous studies, neither longitudinal stability nor fins are mentioned despite these being essential elements of the physics of SWATH vessels. During steady motion, ships acquire dynamic trim and sinkage due to the pressure distribution along the hull. RANS simulations on conventional ships are usually performed with free heave and pitch. However, resistance optimization studies on SWATH ship hulls do not assess longitudinal stability. The choice of free heave and/or pitch is less evident (Begovic et al., 2015; Guan et al., 2020; Ni et al., 2020; Pellegrini et al., 2017). Simulations performed on an unstable geometry would result in a large trim and an overestimated resistance, while SWATH ships usually sails with a zero trim angle thanks to their fins generating lift. When the SWATH ship sails at a high speed, the Munk moment (Lee and Martin, 1976) generates a loss of stability. It is then necessary to add stabilizing fins in order to guarantee pitch and heave stability. RANS calculations on SWATH geometry with different Froude numbers can provide the speed limit for stability (Begovic et al., 2015). The instability is remarkable for speeds where the trim and the resistance increase strongly. It then appears necessary to add corrective appendages to compensate for the loss of stability in SWATH ships.

The seakeeping of the SWATH hull is also an optimization topic. A multi-fidelity optimization method based on surrogate model has been previously by (Bonfiglio et al., 2018) in which Response Amplitude Operators (RAOs) are estimated using 3D Boundary Element Method (high-fidelity) and 2D strip theory (low-fidelity) methods. Some constraints related to displacement and hydrostatics are included in the model. Motions are then estimated in regular and irregular waves, (using the Bretschneider spectrum). Finally, optimal design mitigates motion amplitude and acceleration by more than 25% compared to the initial design. However, potential theory overestimates RAO peaks mainly due to the underestimation of energy dissipation generated by viscous effects (Bonfiglio et al., 2013).

Stabilizing fins and viscous effects play an important role in the prediction of SWATH's motion but are, to the authors' knowledge to date, not considered in the literature. To consider their effects in an optimization loop would make it possible to obtain representative results for the real vessel. This study aims to implement a multi-objective optimization process applied to SWATH ships in order to determine optimal hull design compromises between seakeeping performance and ship resistance, through the consideration of viscous and fin effects. The SWATH ship studied in this paper can operate in waves at zero speed therefore its motion must be low for safety reasons. The ship sails on a wind turbine field, and in the context of fuel economy, resistance should not be overlooked.

As previously mentioned, previous studies focus on only one of these performances (ship resistance or seakeeping) whereas it seems essential to find a compromise between these two objectives, as done in the present work, for the ship use case described here. Previous optimization studies mainly use conventional algorithms to find the optimum. Surrogate models seem to be promising methods for shape optimization (Wackers et al., 2018; Pellegrini et al., 2017; Bonfiglio et al., 2018). In particular, Gaussian process-based regression have shown its effectiveness in the industry (Matheron, 1963) as well as for the mono-objective optimization problem of a hull (Guerrero et al., 2018; Bonfiglio et al., 2018). It therefore seems to be interesting and innovative to apply this type of surrogate-based approach to the multi-objective optimization of an original ship such as a SWATH.

A 50 m SWATH parametric model is hereby considered and the hull is warped according to two parameters: the horizontal semi-axis of torpedoes and the strut inclination angle. The ship displacement remains constant, balanced with the vertical semi-axis of torpedoes. The seakeeping-related objective function is the vertical amplitude of the motion, evaluated using linear potential code. Viscous and fin effects are modeled by adding empirical corrections

into the motion equations. The ship resistance is computed with a finite volume solver using a RANS model. As ship resistance is costly to evaluate, a Gaussian process (GP) surrogate model is used to predict the response of the model over the variability domain, and an iterative multi-objective optimization method using GPs (Passos and Luersen, 2018) is applied to determine the Pareto front. Three levels of fidelity, with increasing computation costs, are considered to model the ship's resistance. In the first low-fidelity level, an indicator of the ship resistance, the wetted surface of the hull, is studied. As a SWATH ship could be vertically unstable at high speeds, the second medium-fidelity level considers with bare-hull ship resistance with free sinkage and fixed trim. The trim is fixed to avoid instability. Finally, the third high-fidelity level, considers stabilizing fins which balance the hydrodynamic pitching moment. Trim angles of the fins are solved to reach moment equilibrium and the fin drag is included in the total ship resistance, which is to be minimized. The multi-objective hull form optimization for a SWATH configuration is solved by considering each fidelity model of the ship resistance. Optimization results provide optimal SWATH hull designs located on the Pareto front, leading to the analysis of optimal hull designs in terms of seakeeping and ship resistance. The geometries obtained using the three fidelity level approaches are compared in order to assess the effectiveness of the low fidelity levels in regard to their computational costs.

The paper structure is as follows. The optimization problem, including the SWATH hull parametric model, is introduced in Section 2. In Section 3, the seakeeping model is presented, while Section 4 provides details on the CFD-based ship resistance model. Section 5 is then dedicated to the multi-objective surrogate-based optimization methods. Results and discussions are presented in Section 6. Finally, the main conclusions of this work are put forward in Section 7.

2. Optimization problem

2.1. Context

The aim of the presented study is to perform a multi-objective optimization of the hull shape of a SWATH ship by taking into account additional considerations that are not considered in previous studies. In particular, longitudinal stability and viscous effects in the prediction of seakeeping performance are modeled in the present paper.

The weight is assumed to be known hence ship displacement ∇, and the position of the center of gravity has been established. In order to maintain compliance with SWATH design rules, a hydrostatic constraint on minimum metacentric height GM_t is implemented.

The ship is an offshore wind farm vessel used for maintenance and staff transfer operations. The optimized quantity related to seakeeping is the amplitude of the vertical motion on a point located on the gangway from the deck to the wind turbine. The significant amplitude of this specific motion, which is evaluated at zero speed in irregular waves, is the first objective to be minimized, while the ship resistance at fixed design speed is the second objective to also be minimized.

2.2. Parametric model

The SWATH hull form configuration is composed of two torpedoes with one single strut (1) on each hull. Torpedoes have two elliptical sections and are composed of a stern (2), a main section (3) which is uniform over its entire length, and a straight bulbous bow (4) (see Figure 1). The waterplane area is fixed and the section of the strut is parabolic as described in (Brizzolara, 2004).

It has been shown in (Latorre and Vasconsellos, 2008) that the strut inclination angle α plays an important role in motion damping as well as on the value of resonance periods. In the present study, the strut inclination angle (see α, Figure 2) is therefore considered and set to vary from $\alpha_{min} = 0°$ to $\alpha_{max} = 45°$. In addition, among existing SWATH ships, several torpedo geometries can be found such as "elephant foot" configuration, "golf club", circular or elliptical sections. The present geometry is provided with elliptical section torpedoes, where the horizontal semi-axis varies from $R_{oymin} = 1.4\,\text{m}$ to $R_{oymax} = 3.0\,\text{m}$ (see R_{oy}, Figure 2). For the remainder of the study, these two parameters are presented in dimensionless form varying from 0 to 1 as follow:

$$R'_{oy} = \frac{R_{oy} - R_{oymin}}{R_{oymax} - R_{oymin}}, \qquad \alpha' = \frac{\alpha - \alpha_{min}}{\alpha_{max} - \alpha_{min}} \tag{1}$$

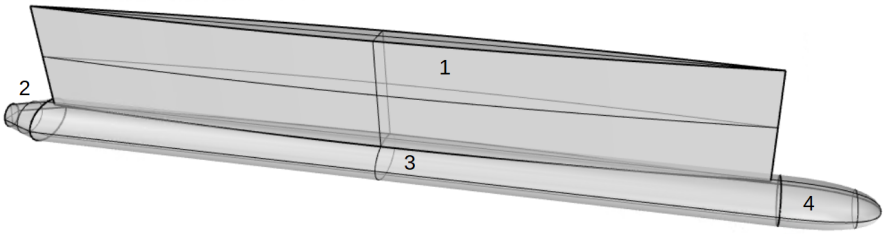

Figure 1: Definition of the port hull. Strut (1), stern (2), main section (3), bulbous bow (4)

Also, the strut inclination angle may decrease the inertia of the waterplane in rotation around the roll axis, and thus the roll metacentric height GM_t. A minimum of $\overline{GM_t} = 1.5\,\text{m}$ is imposed to keep the ship stable in roll. Finally, the vertical semi-axis (see R_{oz}, Figure 2) balances the volume to respect the iso-displacement constraint. The parametric model is configured using Rhino's plug in Grasshopper®, and its main characteristics are summarized in Table 1.

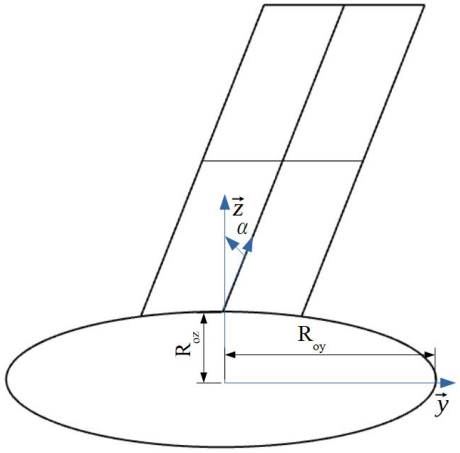

Figure 2: Schematic of the port section with key design parameters: strut inclination angle α, horizontal semi-axis R_{oy} and vertical semi-axis R_{oz}

Parameter	Value	Unit
Length overall L_{oa}	50	m
Hull spacing b	17	m
Draft d	5.5	m
Strut width B_s	2	m
Strut length L_s	40	m
Displacement ∇	1100	m^3
VCG	6.0	m
LCG	24.5	m
Waterplane area A_{wp}	111	m^2

Table 1: Main geometry particulars

3. Seakeeping model

The seakeeping problem is solved using the 3D BEM potential solver HydroStar (Chen, 2011) developed at Bureau Veritas. Energy dissipation in the SWATH hull form is mainly caused by the viscous effects such as vortex shedding. Given that disregarding these effects leads to an overestimation of the RAO peaks (Bonfiglio et al., 2018, 2013), an iterative procedure (Sun et al., 2016) introducing empirical corrections (Lee, 1976) is presently implemented. This procedure is presented in the next following Section 3.1. The Section 3.2 is dedicated to the computation of the vertical motion amplitude in an irregular wave spectrum. The seakeeping model is validated through experiment comparisons in the final Section 3.3.

3.1. Implementation of viscous and fin effects

Within the framework of this study, the amplitude of the vertical motion is evaluated for head seas on a point located along the longitudinal axis (on the symmetry plane of the twin-hull). Roll contribution is neglected, and the ship motion depends solely on heave and pitch motions. Vertical motion equations are as follows,

$$\begin{cases} (M + A_{33})\ddot{\xi_3} + B_{33}\dot{\xi_3} + C_{33}\xi_3 + A_{35}\ddot{\xi_5} + B_{35}\dot{\xi_5} + C_{35}\xi_5 = \Re(F_3 e^{-j\omega t}) \\ (I_5 + A_{55})\ddot{\xi_5} + B_{55}\dot{\xi_5} + C_{55}\xi_5 + A_{53}\ddot{\xi_3} + B_{53}\dot{\xi_3} + C_{53}\xi_3 = \Re(F_5 e^{-j\omega t}) \end{cases} \tag{2}$$

with M, as the mass of the vessel, I_5, as the pitch inertia, C_{ik}, as the restoring force coefficients, ξ_i, as the amplitude of motion in the ith mode (3 for heave, 5 for pitch), F_i as the waves excitation forces and moment, A_{ik} as the added mass coefficients, B_{ik} as the damping coefficients, depending on the circular frequency, which is ω. Those terms include potential, viscous and fin effects as described in (Lee, 1976). The procedure is as follows:

1. Added masses and potential damping are first estimated.
2. Equations of motions are solved to find the amplitude motion.
3. Empirical corrections based on a cross-flow drag approach are added.
4. The procedure is repeated until the amplitude of motion has converged.

The empirical corrections are valid only for horizontal elliptical and circular sections. Therefore, the vertical semi-axis can not be greater than the horizontal semi-axis, i.e. $R_{oz} \leq R_{oy}$.

The forced solution of the linear differential system is sought with its complex expression,

$$\xi_i = \Re(\xi_{i0} e^{-j\omega t}) \tag{3}$$

with ξ_{i0} as the complex amplitude of ξ_i. The system of equations (2) can be written in matrix form and the inversion of the matrix provides the transfer functions in heave RAO_3 and pitch RAO_5. The vertical motion RAO_v is finally built,

$$RAO_v = RAO_3 + xRAO_5 \tag{4}$$

with x as the longitudinal abscissa in the coordinate system centered to the Center of Gravity (CoG).

3.2. Irregular wave response

To reflect as accurately as possible the actual environment that the vessel would operate in, the amplitude of vertical motion is calculated in an irregular wave spectrum. Assuming that the geographic area of operations is the North Atlantic, a JONSWAP spectrum with peak enhancement factor $\gamma = 3.3$ has been chosen. The ship must be operable in waves of significant height $H_s = 3\,\text{m}$. According to NATO data (Huston, 2021), the most likely peak period is $T_p = 9.7\,\text{s}$ for such sea state.

The JONSWAP spectrum S_{JS} (IEC, 2009) is described as:

$$S_{JS} = 0.3125 \cdot H_s^2 \cdot T_p \cdot \frac{f}{f_p}^{-5} \cdot exp[-1.25 \cdot (\frac{f}{f_p}^{-4})] \cdot (1 - 0.287 \cdot log\,\gamma) \cdot \gamma^{exp[-(\frac{\frac{f}{f_p}-1}{4\sigma})^2]} \tag{5}$$

with H_s, as the significant height, $T_p = 1/f_p$ as the peak period, σ as the spectral width, $\sigma = 0{,}07$ for $f \leq f_p$ and $\sigma = 0{,}09$ if $f > f_p$. Response spectrum in irregular waves S_v is then calculated, following

$$S_v = |RAO_v|^2 S_{JS} \tag{6}$$

Finally, the significant amplitude η_v is estimated using the moment of 0^{th} order m_{0v}, whereby

$$m_{ov} = \int_0^{+\infty} S_v d\omega \tag{7}$$

$$\eta_v = 2\sqrt{m_{ov}} \tag{8}$$

3.3. Comparison and validation with experimental data

Seakeeping tests were performed at the MARIN (Maritime Research Institute Netherlands, (Abeil, 2017)) on the *Windkeeper* SWATH ship. Figure 3 shows a sample of the 3D panel distribution of the geometry used for the BEM simulations. The ship was tested in regular waves (Amplitude Amp = 1 m) and irregular waves (JONSWAP spectrum whereby $H_s = 1.5\,\text{m}$ $T_p = 9.5\,\text{s}$). Within the scope of this study, only the amplitude of vertical motion in two points located along the longitudinal axis are studied. In Figure 4a and Figure 4b, the first peak of amplitude is attributable to heaving motion (resonant frequency of $0.6\,rad.s^{-1}$), which is perhaps not sufficiently damped since the amplitude of motion is a bit higher than expected in regular waves at x = 19 m (see Figure 4b). The second peak of amplitude is attributable to pitch motion but there is no measure in regular waves at the interesting frequency ($0.85\,rad.s^{-1}$). A difference of amplitude between numerical RAOs (Present) and experimental data in irregular waves (Exp $H_s = 1.5\,\text{m}$ $T_p = 9.5\,\text{s}$) should be found as the response of motion is not linear with the wave amplitude. However, the curves match, and the trend is correctly captured as well as the periods of resonance. Therefore, the modeling is sufficient given the expected results for a potential code and empirical corrections (Lee, 1976).

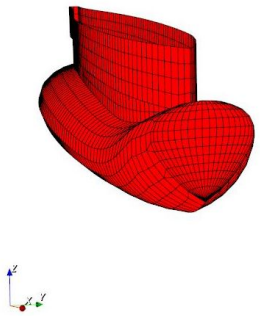

Figure 3: 3D panel distribution of the reference SWATH

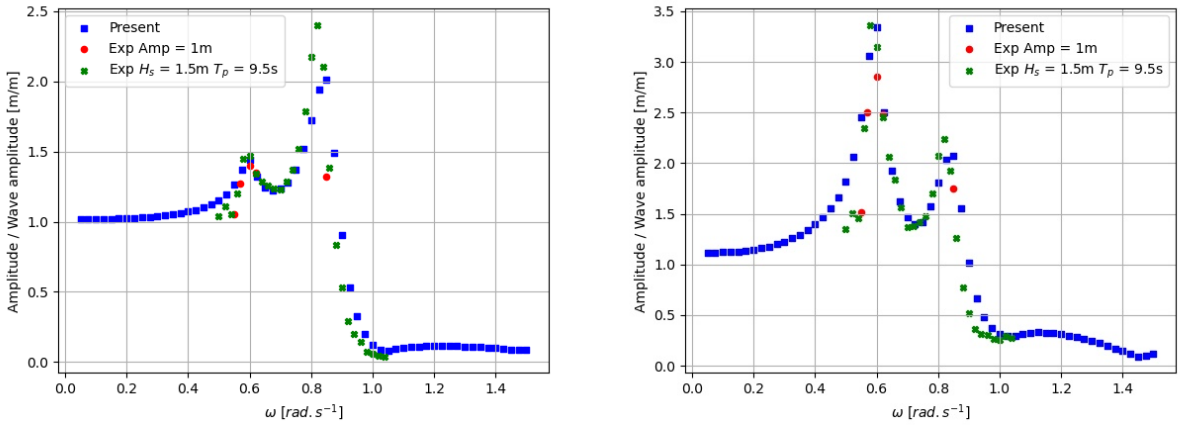

(a) (b)

Figure 4: Comparison of the RAOs of the vertical amplitude at various locations x = 3.3 m (a) and x = 19 m (b), between MARIN experimental results (Abeil, 2017) in regular waves with an of amplitude 1 m (Exp Amp = 1 m), in irregular waves modeled by a Jonswap spectrum (Exp H_s = 1.5 m, T_p = 9.5 s) and numerical simulations (Present)

4. Ship resistance

4.1. RANS simulation

Ship resistance is evaluated using the finite-volume solver ISIS-CFD (Queutey and Visonneau, 2007) developed at ECN-CNRS. A RANS method with a k-ω SST (Shear Stress Transport) turbulence model is used. SWATHs ships sail at high Froude number (0.4-0.9) (Yun et al., 2019). A sailing speed of 20 kt (Fr = 0.46) is chosen for the present study. Initially, the sinkage is free while trim is fixed to 0°, to avoid instability.

An intermediate geometry is created, with R'_{oy} = 0.5 and α' = 0.33, to study the influence of the mesh density and the domain size on the resistance value. Using the symmetry of the problem, only half geometry is modeled. The mesh is created with the semi-automated unstructured hexahedral mesh generator HEXPRESS^{TM} within the Numeca CFD package.

The reference domain is 4 L_{oa} long, 2 L_{oa} wide, and 1,25 L_{oa} high. A mesh with approximately 1.4 million cells is shown in Figure 5. Refinement on the hull and the free surface enhances mesh density. The domain is enlarged by increasing bounds in x and y directions. The flow within the boundary layer is solved using wall functions with a mesh size close to the wall such as y_+ = 100. Simulations are performed on 64 cpus.

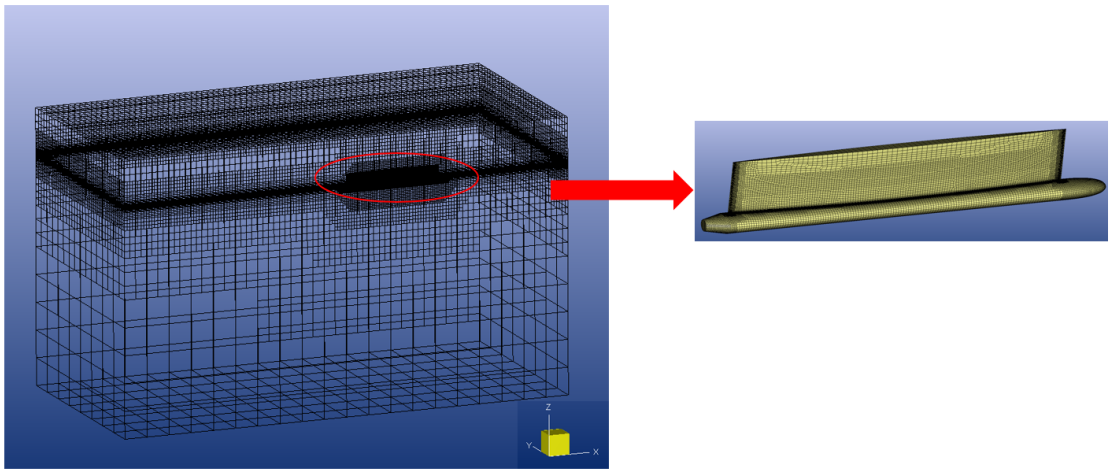

Figure 5: Computation domain and zoom on the mesh of the reference geometry

Figure 6 shows that mesh density and domain size have little effect on ship resistance. A maximum relative difference of 1.5% is found for a domain 1.5 larger in x and y. Furthermore, sinkage convergence is studied (Figure 6). A maximum relative difference of 5.9% is found with the medium mesh (2.1M cells) while domain size has a lesser effect on sinkage. However, variations in sinkage hardly impact resistance which converges more quickly. As resistance is one of the objective functions, the reference mesh (1.4M cells) is chosen for the optimization loop and convergence criteria based on resistance is settled.

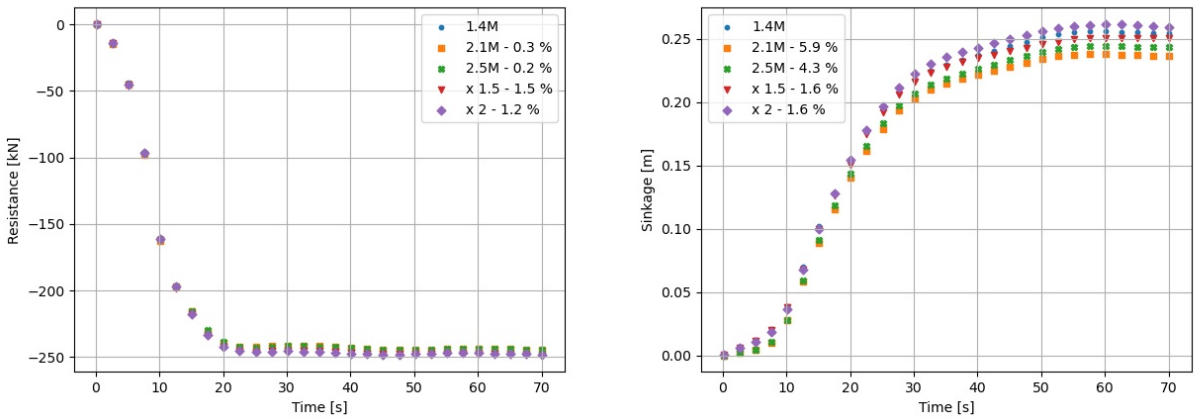

(a) (b)

Figure 6: Time variations of R_t (a) and Sinkage (b) for different mesh densities (1.4M, 2.1M, 2.5M) and mesh sizes (x 1.5, x 2). Relative differences with the reference mesh (1.4M) are specified

4.2. Influence of the symmetry plane

In order to reduce the computational cost, it was chosen to model only one hull using a symmetry plane boundary condition on the y_{min} plane. This approximation is used in various SWATH optimization studies (see Guan et al. (2020), Lin et al. (2019), Ni et al. (2020)). However, there may be interference between the waves of the two hulls.

Thus, in order to justify the use of this simplification, we propose to compare the results of RANS simulations of the reference mesh, determined in the previous section, when considering the symmetry plane boundary condition or the complete model including the twin hulls.

The total ship resistance R_t and the wave resistance R_w are compared in Table 2, as well as the wave patterns in Figure 7. There is about 1% difference in total resistance between the two configurations. Furthermore, the comparison of wave patterns shows that there is no significant difference justifying the use of the twin hulls model. It is thus clearly shown that the use of the symmetry plane boundary condition is well adapted for this configuration.

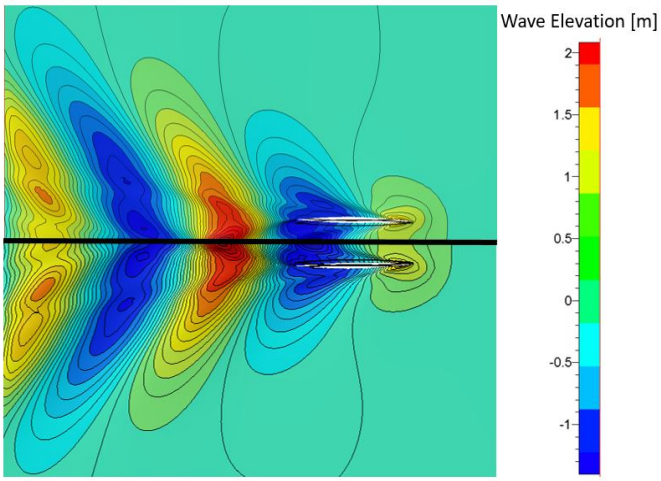

Figure 7: Comparison of the wave pattern using the symmetry plane (upper part) and the twin hulls (lower part)

Resistance	Symmetry plane	Twin hulls
R_w	344 kN	348 kN
R_t	488 kN	492 kN

Table 2: Ship resistance comparison with and without symmetry plane

4.3. Longitudinal stability

The mesh and domain convergences have been conducted without assessing the longitudinal stability. However, slender bodies such as torpedoes are subject to the destabilizing Munk moment. Among the panel of geometries that could be calculated during the optimization loop, the speed limit for stability is estimated according to the longitudinal stability condition (Lee and Martin, 1976).

The so-called Munk moment M_m (Faltinsen, 1990) can be expressed, as

$$M_m = -\frac{1}{2}(A_{33} - A_{11})sin(2\theta)U^2 \tag{9}$$

with U as the forward speed of the vessel. For small trim angle θ, Eq. (9) can be linearized with,

$$M_m \approx -(A_{33} - A_{11})\theta U^2 \tag{10}$$

M_m is then added into the equation of the pitch motion (Eq. (2)). According to Routh criteria (Lee and Martin, 1976), system (2) is stable if,

$$C_{33}(C_{55} - (A_{33} - A_{11})U^2) - C_{35}C_{53} > 0 \tag{11}$$

Also, $C_{55} \gg C_{35}$ C_{53}/C_{33} (Lee and Martin, 1976) and $A_{33} \gg A_{11}$ for SWATH ship(A_{33} / A_{11}= 20 for the *Windkeeper*). The speed limit of stability is finally given by,

$$U_{lim} = \sqrt{\Delta \frac{gGM_l}{A_{33}}} \tag{12}$$

with GM_l as the longitudinal metacentric height, Δ as the mass of the ship and g as the acceleration of gravity. Formula (12) has been verified and compared to numerical simulations, calculating the speed limit for stability (Hooijmans, 2016), (Bigi, 2018) where a relative difference of less than 2% has been found.

4.4. Configuration of RANS simulations

To better assess the speed limit for stability of SWATH hull geometries candidates, a surrogate model of U_{lim} as function of the two hull variables is constructed. This is achieved by using a Gaussian process surrogate model (Krieg, 1951) that is built using 15 sampled geometries with a Latin Hypercube Sampling (LHS) (Mckay et al., 1979). The prediction of U_{lim} over the variability domain is given in Figure 8. Further details on the surrogate models are provided in Section 5.

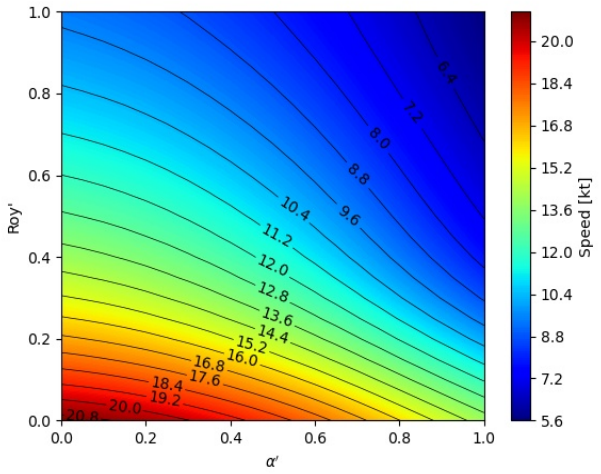

Figure 8: Mean prediction of U_{lim} as a function of design parameters (α', R'_{oy})

The predicted speed limit (see Figure 8) decreases as the angle and semi-axis increase. Figure 8 shows that, given the present variability domain, almost all geometries are unstable. Indeed, the predicted speeds limit are lower than 20kt, except those located in the bottom left corner. It is thus necessary to fix pitch motion during resistance calculations or to consider fins. Sinking will not cause instability and can therefore be let free.

SWATH ships usually sail at zero trim angle, and so fins must generate lift enough to compensate Munk moment. To balance the hydrodynamic moment along the pitch axis, forward and aft fins are added to the geometry (see Figures 9 and 10). Their main geometrical dimensions are listed in Table 4.4. In all computations of the ship resistance R_t, the pitch motion is still fixed, and the trim is 0°. In the medium-fidelity level, fins are not taken into consideration.

In the highest-fidelity model, a stationary solution of the hull equilibrium is sought. The hydrodynamic moments of the hull and fins calculated at the center of gravity are therefore post-processed during the simulation to compute the sum of these moments every 10 time steps. In order to solve the balance on the sum of the moments, the Angle of Attack (see AoA, Figures 9 and 10) of the fins is adapted, every 10 time steps, using a dichotomy method. In short, if the lift of the foils is not sufficient to balance the ship, the AoA is increased, otherwise it is decreased. This approach has the benefit of allowing robust RANS calculations of the ship's resistance using a fixed ship trim. No deformation of the mesh is therefore necessary, which saves computational costs and preserves the good quality of the mesh.

In order to allow fins rotations during RANS calculations, a sliding mesh method is considered. As shown in Figures 11 and 12, the foils are located in their own meshed domain (see cylindrical domains in red) which is included in the overall domain. A particular caution has been made regarding the size of the mesh at the interface between the two domains (see Figure 12) to conserve a smooth transition and preserve the quality of the interpolations.

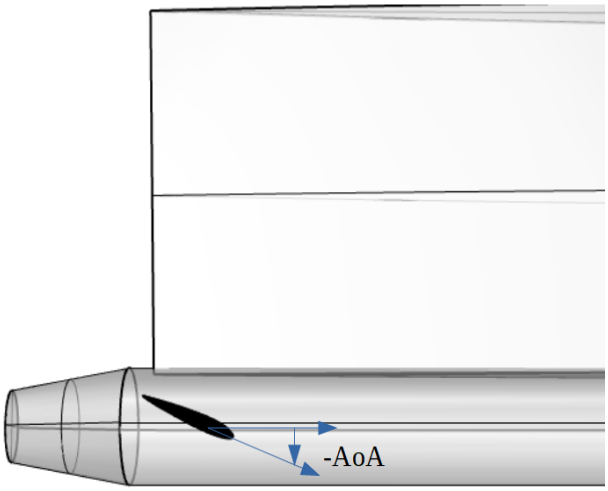

Figure 9: Schematic of the aft foil

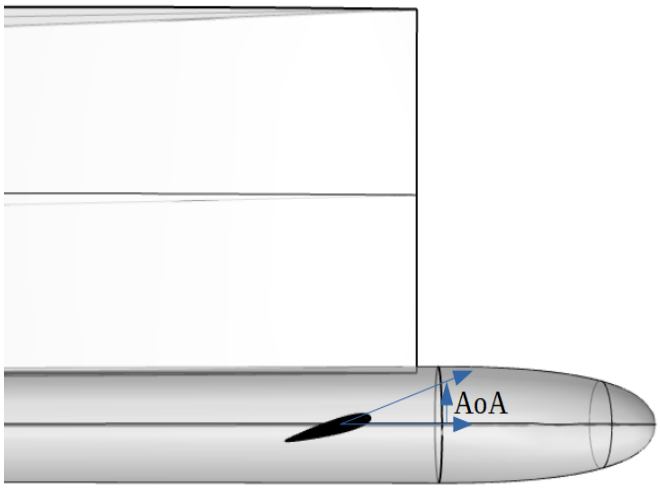

Figure 10: Schematic of the forward foil

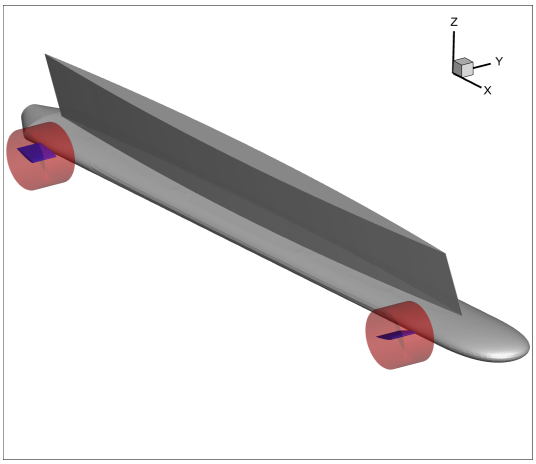

Figure 11: Port hull with its two foils in their compartment allowing the sliding mesh

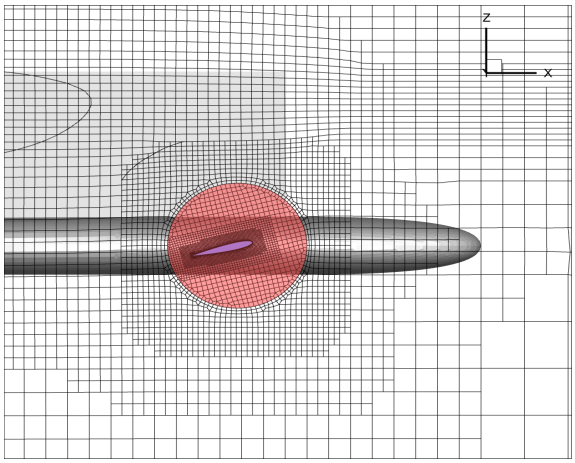

Figure 12: Sliding mesh of the forward foil

Characteristic	Value
Chord	1.75 m
Span	2.2 m
Profile	NACA 0012
Location from CoG	± 18.5 m

Table 3: Main fins dimensions

Finally, the optimization problems considered in this study are provided below. The problem (13) concerns the first (low) fidelity level, while problem (14) is for the second (medium) and third (high) fidelity levels.

$$\min_{\boldsymbol{x}\in\Omega} \eta_v(\boldsymbol{x}),\mathrm{S}(\boldsymbol{x}) \quad \text{s.t.} \begin{cases} \nabla = 1100\ \mathrm{m}^3 \\ \overline{GM_t} \geq 1.5\ \mathrm{m} \\ \mathrm{R_{oz}} \leq \mathrm{R_{oy}} \end{cases} \tag{13}$$

$$\min_{\boldsymbol{x}\in\Omega} \eta_v(\boldsymbol{x}),\mathrm{R_t}(\boldsymbol{x}) \quad \text{s.t.} \begin{cases} \nabla = 1100\ \mathrm{m}^3 \\ \overline{GM_t} \geq 1.5\ \mathrm{m} \\ \mathrm{R_{oz}} \leq \mathrm{R_{oy}} \end{cases} \tag{14}$$

In both optimization problems (13) and (14), design parameters are $\boldsymbol{x} = \left(\mathrm{R_{oy}}, \alpha\right)$ and the design domain is set to $\Omega = [1.4\ \mathrm{m}, 3\ \mathrm{m}] \times [0°,45°]$. The dimensionless domain is then $\Omega' = [0,1]^2$

5. Multi-objective surrogate-based optimization

We consider optimization problems, where several objectives have to be minimized simultaneously over a design variable $\Omega \subset \mathbb{R}^d$:

$$\min_{\boldsymbol{x}\in\Omega} f_1(\boldsymbol{x}),\ldots,f_m(\boldsymbol{x}) \quad \text{s.t.} \quad \boldsymbol{g}(\boldsymbol{x}) \leq 0 \tag{15}$$

where $\boldsymbol{x} = (x_i)_{1\leq i\leq d}$ is a vector of design variables, $\boldsymbol{f} = \left(f_j\right)_{1\leq j\leq m}$ is a vector of objective functions to be minimized ($f_i : \Omega \mapsto \mathbb{R}$), and $\boldsymbol{g} = (g_k)_{1\leq k\leq p}$ is a vector of inequality constraints ($g_k : \Omega \mapsto \mathbb{R}$). The existence of an optimal solution, minimizing all objectives at once is not typically granted. This leads to the search for an optimal set of solutions, called the Pareto front. According to the Pareto domination rule (Fonseca and Fleming, 1998), $\boldsymbol{x} \in \Omega$ is said dominated by $\boldsymbol{x'} \in \Omega$ if for all $1 \leq j \leq m$, $f_j(\boldsymbol{x'}) \leq f_j(\boldsymbol{x})$, and $\boldsymbol{g}(\boldsymbol{x'}) \leq 0$. The set of optimal (non-dominated) design vectors, to be determined in Ω, is then referred to as the Pareto set. Evolutionary algorithms (Deb et al., 2002; Coello et al., 2007) have been demonstrated to be well-adapted for solving multi-objective problems in real-word applications with moderate objective computation cost (Huang et al., 2015; Lim and Kim, 2019).

In the present work, individual evaluations of the objective functions are assumed to be numerically very expensive. A common approach is then to use surrogate models in place of $\boldsymbol{f}$ to reduce the computational burden associated with the evaluations of $\boldsymbol{f}$ (Simpson et al., 2001). Gaussian processes (GP) (Rasmussen and Williams, 2006; Kleijnen, 2009) are presently considered, which, owing to their statistical nature, provide both a prediction value and a measure of the uncertainty (variance) for each objective function in this prediction. These features are appealing within the context of optimization, as they can be exploited to derive rigorous optimization strategies, by evaluating sequentially the computer models at design vectors that maximize a so-called merit function (Picheny et al., 2013).

In mono-objective problems, GP-based approaches are globally referred to as Efficient Global Optimization (EGO) (Jones et al., 1998), whereby the merit function is based on an Expected Improvement (EI) criterion, expressing a trade-off between sampling in promising regions and exploring in unsampled regions. EGO has been successfully applied to complex optimization problems, such as non-linear fluid-structure interaction problems (Sacher et al., 2017, 2018) or RANS computations (Meliani et al., 2019).

Over the last few years, surrogate-based approaches have also been proposed to address the multi-objective problem. Indeed, several GP-based multi-objective optimization strategies propose to extend the EI infilling criterion of Jones et al. (1998). The definition of the improvement can then be considered over the Pareto front (Wagner et al., 2010), using for instance, Maximin distance (Svenson and Santner, 2010), Euclidean distance (Keane, 2006), or the well-known Hypervolume infilling criterion (Emmerich et al., 2006, 2011; Luo et al., 2014). Recently, merit functions aimed at computing and reducing uncertainty of the predicted Pareto front have been developed (Picheny, 2015;

Binois et al., 2015; Passos and Luersen, 2018). In particular, Passos and Luersen (2018) have proposed and validated, on a real-world composite panel application, the efficiency of a new merit function: Minimization of the Variance of the Predicted Front (MVPF). In the present work, the MVPF approach is applied to solve the SWATH hull form optimization problem, using the "moko" open-source R package (Passos and Luersen, 2018).

In Section 5.1, we shall summarize the construction of the GP model for an objective function f_j. The MVPF infilling criterion is then given in Section 5.2. Section 5.3 presents a Median Compromise of the Pareto Front (MCPF) criterion, which can be used to monitor the convergence of the optimization resolution, in addition to providing a median trade-off selection of the optimal design vector located on the Pareto front. The last Section 5.4 provides the Inverse Generational Distance (IGD) metric, which can be used to quantify the quality of Pareto sets.

5.1. GP surrogate construction

In the present Section 5.1, the GP surrogate construction of an objective function f_j is provided. The method is identical for the GP surrogate construction of an inequality constraint function g_k.

We consider a set of n training points $\mathcal{X} = (\boldsymbol{x}_1, \ldots, \boldsymbol{x}_n)$, each in Ω. The training points are associated to the vector $\mathcal{Y}^{(j)} = (y_1^{(j)}, \ldots, y_n^{(j)})$ of noisy observations of the objective function f_j. It is assumed that $y_i^{(j)} = f_j(\boldsymbol{x}_i) + \epsilon_i^{(j)}$, where the $\epsilon_i^{(j)}$ are independent and identically distributed Gaussian random variables having zero-mean and variance $\sigma_{\epsilon_j}^2$.

The GP construction considers that $f_j(\boldsymbol{x})$ is a realization of a zero-mean multivariate Gaussian process with covariance function C_j. We consider here the Matérn $5/2$ covariance function defined, in its univariate form, by

$$c(x,x';l) \doteq \left(1 + \sqrt{5}\frac{|x-x'|}{l} + \frac{5}{3}\left(\frac{|x-x'|}{l}\right)^2\right)\exp\left(-\sqrt{5}\frac{|x-x'|}{l}\right) \tag{16}$$

leading to the definition of the multidimensional covariance function as,

$$C_j\left(\boldsymbol{x},\boldsymbol{x}';\Theta_j\right) \doteq \prod_{i=1}^{d} c(x_i,x_i';l_i) \tag{17}$$

where $\Theta_j = \left(l_1^{(j)}, \ldots, l_d^{(j)}\right)$ is the vector of covariance hyper-parameters to be inferred from the $\mathcal{Y}^{(j)}$ observations. From the conditional rules of joint Gaussian distributions (Rasmussen and Williams, 2006), the *best* prediction $\widehat{f_j}(\boldsymbol{x})$ of $f_j(\boldsymbol{x})$, *i.e.*, the mean of $y^{(j)}$, and the prediction variance $\widehat{\sigma_j}^2(\boldsymbol{x})$ are given by,

$$\widehat{f_j}(\boldsymbol{x}) = \boldsymbol{k}_j^{\mathrm{T}}(\boldsymbol{x})\left(\boldsymbol{C}_j\left(\Theta_j\right) + \sigma_{\epsilon_j}^2\boldsymbol{I}\right)^{-1}\mathcal{Y}^{(j)} \tag{18}$$

$$\widehat{\sigma_j}^2(\boldsymbol{x}) = \kappa_j(\boldsymbol{x}) + \sigma_{\epsilon_j}^2 - \boldsymbol{k}_j^{\mathrm{T}}(\boldsymbol{x})\left(\boldsymbol{C}_j\left(\Theta_j\right) + \sigma_{\epsilon_j}^2\boldsymbol{I}\right)^{-1}\boldsymbol{k}_j(\boldsymbol{x}) \tag{19}$$

In (18) and (19) we have denoted $\boldsymbol{C}_j \in \mathbb{R}^{n\times n}$ the symmetric covariance matrix of the training points, $\kappa_j(\boldsymbol{x}) \doteq C_j\left(\boldsymbol{x},\boldsymbol{x};\Theta_j\right)$, $\boldsymbol{k}_j(\boldsymbol{x}) \doteq \left(C_j\left(\boldsymbol{x},\boldsymbol{x}_1;\Theta_j\right)\cdots C_j\left(\boldsymbol{x},\boldsymbol{x}_n;\Theta_j\right)\right)^{\mathrm{T}}$ the covariance vector between the observations in $\mathcal{X}$ and $\boldsymbol{x}$, and $\boldsymbol{I}$ the identity matrix of $\mathbb{R}^n$. The hyper-parameters Θ_j and noise variance $\sigma_{\epsilon_j}^2$ can be determined by maximizing the log-marginal likelihood (see Rasmussen and Williams (2006) for more details).

5.2. Minimization of the Variance of the Predicted Front (MVPF)

The MVPF infilling criterion, proposed by Passos and Luersen (2018), aims at improving the fidelity of the predicted Pareto front. A Pareto front is generated thanks to a state-of-the-art multi-objective constrained optimization algorithm (such as NSGA-II (Deb et al., 2002)) and using GP surrogate predictions (one for each objective and constraint function, see Eq. (18)) as input functions. The MVPF criterion then consists of selecting a design vector variable $\boldsymbol{x}_{MVPF}$ from the Pareto set $\mathcal{X}_{PF}$, to be evaluated. This selection is based on the highest predicted variances in objective functions (see Eq. (19)), and is written as,

$$\boldsymbol{x}_{MVPF} \doteq \underset{\boldsymbol{x}\in\mathcal{X}_{PF}}{\arg\max}\left(\prod_{j=1}^{m}\underline{\widehat{\sigma_j}^2}(\boldsymbol{x})\right) \tag{20}$$

where $\widehat{\sigma_j}^2(\boldsymbol{x}) \in [0,1]$ is the normalized predicted variance (from Pareto set). The design vector $\boldsymbol{x}_{MVPF}$ is added to $\mathcal{X}$, and finally $\boldsymbol{f}$ and $\boldsymbol{g}$ are computed. A new iteration can then start by updating GP models with the new observations, and the iterative process is repeated until a stopping criterion is reached. For more details on the MVPF algorithm, we refer readers to (Passos and Luersen, 2018).

5.3. Median Compromise of the Pareto Front (MCPF)

Solving multi-objective optimization problems leads to the search for an optimal set of solutions (i.e., Pareto front). In most real-word applications, a design vector from the Pareto set must be selected to provide an optimal design choice. This selection is therefore a compromise choice, which is usually based on the knowledge of the designer. With the aim of avoiding this compromise selection by the designer, the MCPF criterion is proposed in this study, and is provided by,

$$\boldsymbol{x}_{MCPF} \doteq \underset{\boldsymbol{x}\in\mathcal{X}_{PF}}{\arg\min}\left(\sum_{j=1}^{m} \arg\operatorname{sort}\left(\widehat{\boldsymbol{f}}_{PF_j}, \widehat{f}_j(\boldsymbol{x})\right)^2\right) \tag{21}$$

where, $\arg\operatorname{sort}(\boldsymbol{f},f) \doteq \left\{q \in \{1,\ldots,t\} \mid f < f_q \in \boldsymbol{f}\right\}$ and $\widehat{\boldsymbol{f}}_{PF_j}$ is the vector of objective function j predictions on the Pareto set $\mathcal{X}_{PF}$, which is composed of t non-dominated design vectors. As can be seen in Eq. (21), the median trade-off is selected by considering the rank, from the Pareto set, of each objective function prediction. This definition allows a design vector compromise to be determined without the need for weights or scaling of objective function values. In the following, the MCPF criterion is used to compare results and monitor the convergence of optimization resolutions.

5.4. Inverted Generational Distance (IGD)

The Inverted Generational Distance (IGD) metric (Shimoyama et al., 2013) can be used to monitor the quality (Passos and Luersen, 2018) of Pareto sets along the optimization process. Indeed, the IGD provides the average distance between all designs in the true set and the closest design of the current set. IGD is defined as,

$$IGD(\mathcal{X}_{PF_T},\mathcal{X}_{PF}) \doteq \frac{1}{t}\sum_{\boldsymbol{x}'\in\mathcal{X}_{PF_T}} \min d(\boldsymbol{f}(\boldsymbol{x}'),\boldsymbol{f}(\boldsymbol{x}))_{\boldsymbol{x}\in\mathcal{X}_{PF}} \tag{22}$$

where $\mathcal{X}_{PF_T}$ and $\mathcal{X}_{PF}$ are the true and current Pareto sets and $d(\cdot)$ is the Manhattan distance metric. The quality of the Pareto set therefore increases when the IGD decreases. In the present work, the IGD convergence is computed at the end of optimization resolutions and the last obtained Pareto set is considered as the "true" Pareto set.

6. Results and discussions

The aim of this paper is to introduce a multi-objective optimization method of SWATH ships using three levels of fidelity. The significant amplitude of the vertical motion is minimized as well as the resistance. In the first low fidelity level, the wetted surface is the main parameter to assess the ship resistance. RANS simulations are then used to compute the resistance in the second and third fidelity levels. The second level considers the resistance without fin effects, while stabilizing fins are modeled in the third level. Optimization processes are performed with the same LHS composed of 15 observations.

6.1. Low-fidelity level: Wetted surface

In this first optimization problem of low fidelity, for the ship resistance, the number of iterations is set to 100. At each iteration, the Pareto front is built to find the median compromise (see Section 5.3). Its design parameters and values of the objective functions are plotted in terms of the iteration number in Figure 13 to better appreciate the convergence of the optimization. The median compromise is quite stable, and from iteration 30, we can see that the objective functions and design parameters are almost converged. There are some oscillations (iterations 48, 55, 99, and 100) that slightly alter S (see Figure 13c), but not at all η_v (see Figure 13b).

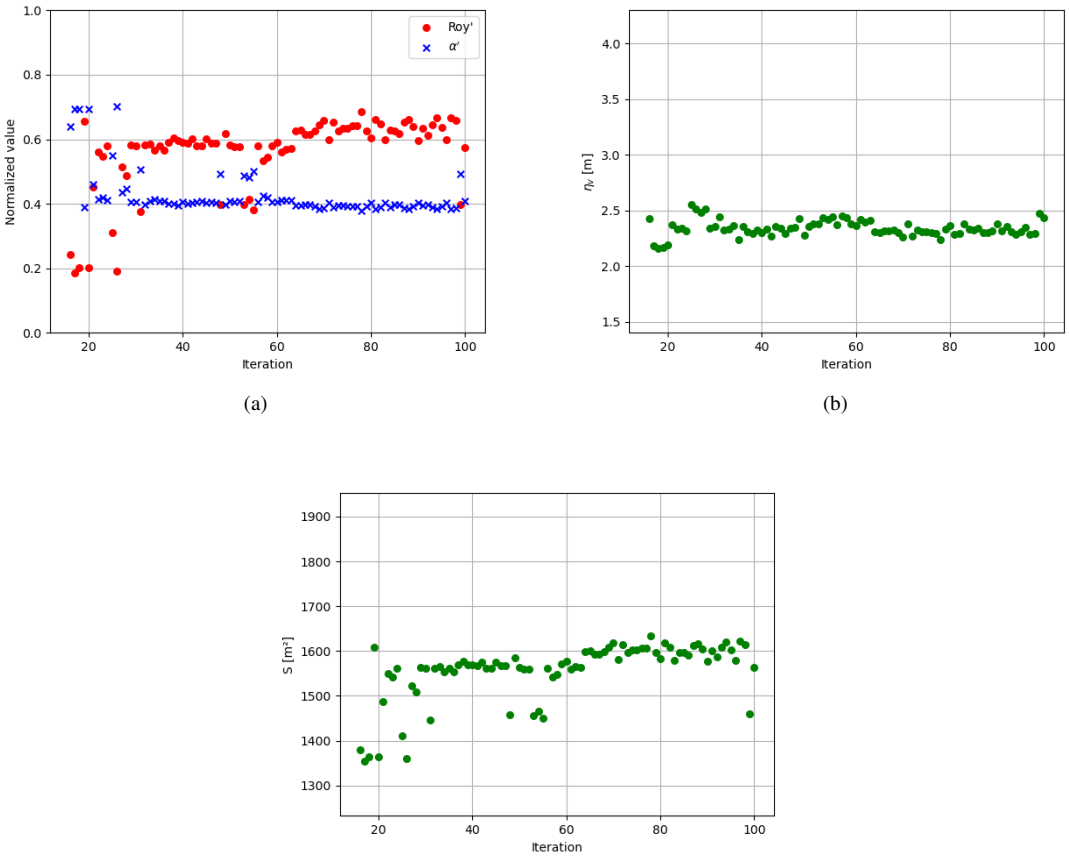

Figure 13: Iterative variation of design parameters α'and R'_{oy} (a) and objective functions values of the median compromise η_v (b) and S (c) - Low fidelity level

As mentioned in 5.4, the Inverted Generational Distance compares two Pareto fronts to assess its quality and convergence. Here, the IGD is plotted in terms of the iteration number, where the last PF being the "true" Pareto front. Figure 14 shows that IGD is decreasing towards zero, leading to the convergence of the Pareto front.

Results at the last iteration are given in Figures 15, 16, 17, 18. The mean surrogate prediction of both objective functions is plotted on the variability domain, as well as the Pareto front in 3D. Feasible and unfeasible calculation points are distinguished, allowing to observe the restriction domains of the constraints.

In Figure 15, η_v is a multi-modal function. Several minima are found on the top right of the graph, where the constraints are not respected. A maximum is also found on the lower boundary of the horizontal semi-axis. However, geometries with R'_{oy} lower than 0.19 have an upward-facing elliptical section (i.e. $R_{oy} < R_{oz}$). The seakeeping model is not valid in such a range so the prediction of η_v must be handled with care. Torpedoes are closed to the free surface and amplitude of motion grows. The multi-modal character of η_v is illustrated in Figure 18, where we can see that the PF is discontinuous. These discontinuities explain the oscillations in the convergence of the median compromise (see Figures 13). The position of the median compromise alternates between two discontinuous branches of the Pareto Front, at a value of approximately S = 1500 m^2.

The front is bounded by the constraints. One branch is located on $R'_{oy} = 0.19$, whereby condition (13) is no longer respected under this value. The other branch is located on the diagonal of the variability domain, $\overline{GM_t}$ being lower than 1.5 m on the right side of the domain. (see Figures 15,16, 17). Increasing α' and R'_{oy} lead to a decrease of the

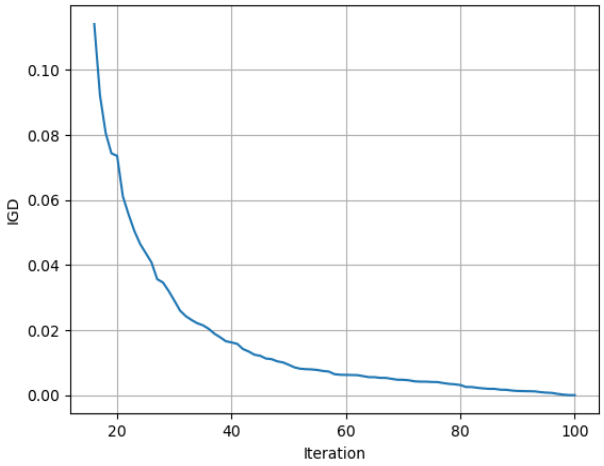

Figure 14: Iterative variation of the Inverted Generational Distance - Low fidelity level

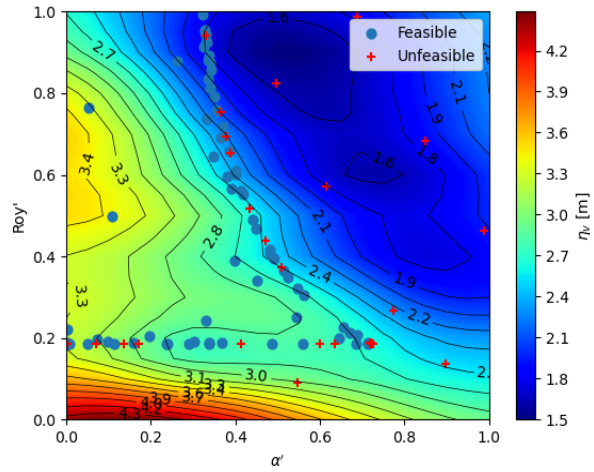

Figure 15: Mean prediction of η_v as a function of design parameters $(\alpha', R'_{oy}) \in \Omega'$

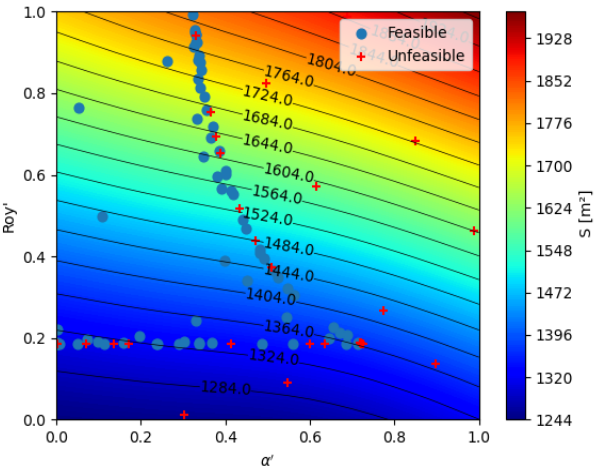

Figure 16: Mean prediction of S as a function of design parameters $(\alpha', R'_{oy}) \in \Omega'$

amplitude of motion (Figure 18) but raises S (Figures 16). Geometries with vertical struts and small R'_{oy} have a lower S but in return, their motions are more important. Therefore, S and η_v are indeed opposite functions, this justifies the interest in using a multi-objective optimization algorithm to find the median compromise. Torpedoes with large R'_{oy} provide more damping and added mass. Also, resonant period is longer than period of circular section, and so are further from the peak amplitude of the wave spectrum.

To better appreciate the relationship between the geometry and the value of the objective functions, the sections of the geometries which minimize η_v, S and the best compromise are compared in Figure 19. The characteristics of the median compromise from the last iteration are listed in Table 4. Between the blue (low S) and the red geometry (low η_v) presented in Figure 19, η_v and S can be respectively decreased by 46% and 26%. These numbers show that performance could drastically evolve from one optimum to another. It is therefore necessary to define a design compromise.

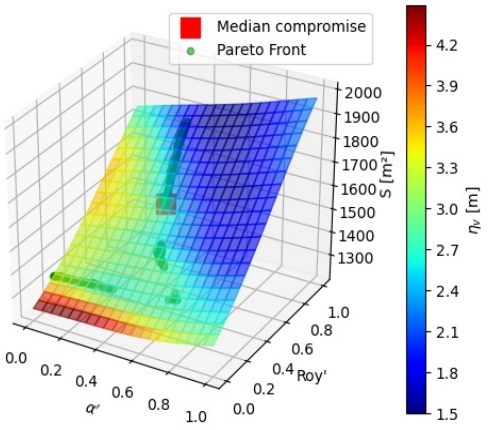

Figure 17: Mean prediction of the objective functions, Pareto Front and median compromise as a function of design parameters $(\alpha', R'_{oy}) \in \Omega'$ with S in vertical axis and η_v in color - Low fidelity level

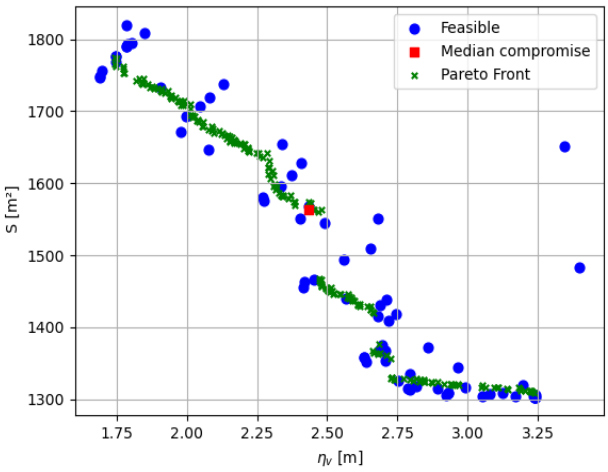

Figure 18: Objective functions values of the Pareto Front, median compromise and feasible designs - Low fidelity level

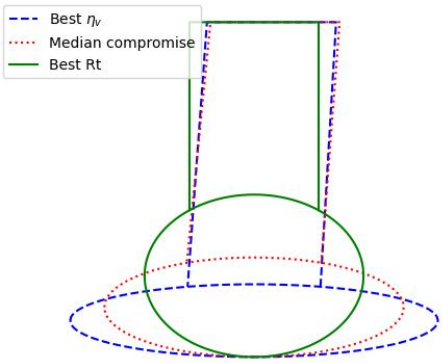

Figure 19: Cross-sectional diagram of the geometries with the best η_v, the median compromise and the best S - Low fidelity level

Characteristic	Value
(α', R'_{oy})	(0.41, 0.57)
η_v	2.43 m
S	1563 m^2

Table 4: Characteristic of the median compromise - Low fidelity level

6.2. Medium fidelity level: Bare hull resistance - free sinkage, fixed trim & no fin

The speed limit study (see Figure 8) shows that all geometries are unstable. To avoid instability, sinkage is free while trim is fixed. Let the pitch motion free could lead to unexpected large trim angle and resistance which is not representative of actual sailing conditions of SWATH ships and may cause instabilities. This second level of fidelity for the resistance deals with the bare hull resistance regardless the fin effects. Convergence of the median compromise is studied in the same way as in the first case. Figures 20 show the convergence of the design parameters and objective functions of the median compromise.

As the prediction of η_v remains of the same nature, the PF is still discontinuous and there are some oscillations on the location of the median compromise (iterations 39, 40, see Figures 20). The median compromise is located in the same range ($(\alpha', R'_{oy}) \approx (0.4, 0.6)$). The IGD (see Figure 21) tends to zero, which also confirms the convergence.

Results at the last iteration are presented in Figures 22 and 23. The seakeeping calculation has not changed so the mean prediction of η_v is similar. Slight differences are explained by the noise of the prediction as well as the difference in calculation points. Figure 22 shows the mean prediction of R_t. Bare hull resistance is mainly impacted

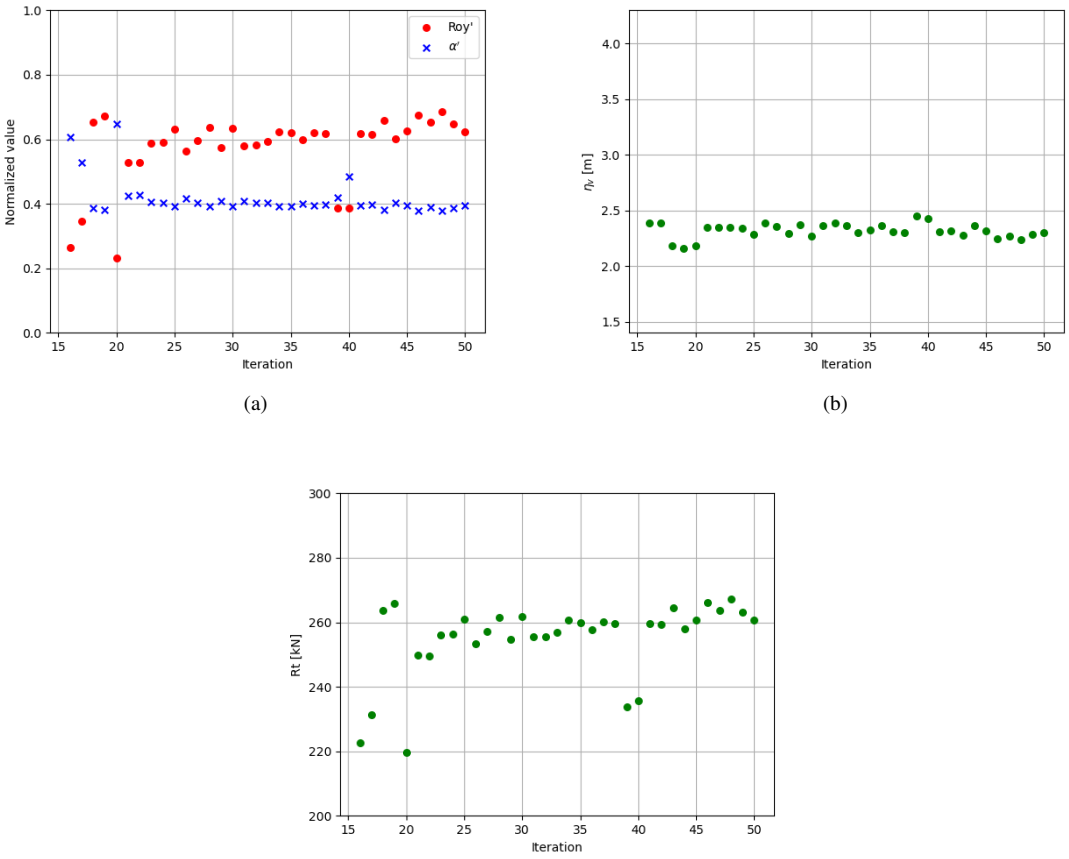

Figure 20: Iterative variation of design parameters α'and R'_{oy} (a) and objective functions values of the median compromise η_v (b) and R_t (c) - Medium fidelity level

by the change of section of torpedoes while inclination angle is less critical. A minimum is found around the domain where the constraint on the semi-axis is not respected ($R'_{oy} \approx 0.1$). The hull volume is closer to the free surface that could increase the wave resistance, therefore R_t increases again for very low horizontal semi-axis ($R'_{oy} < 0.1$).

R_t and S evolve in the same way as shown in Figure 16. The wetted surface is a good indicator of the resistance for a SWATH, particularly when the hull is deeply immersed. The PF is still discontinuous (see Figure 23) and the median compromise remains within the same range (see Figure 20).

The sections of the geometries which minimize η_v, R_t and the best compromise are compared in Figure 24. These geometries are very close to those of the first case (see Figure 19). This means that the first level of fidelity is accurate for this optimization problem. The median compromise is referenced in Table 5. Geometries can also be compared: between the blue and the red geometry presented in Figure 19, η_v and R_t can be respectively decreased by 41% and 28%.

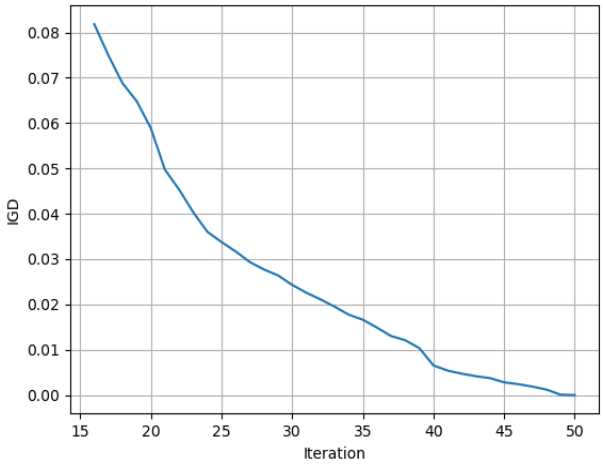

Figure 21: Iterative variation of the Inverted Generational Distance - Medium fidelity level

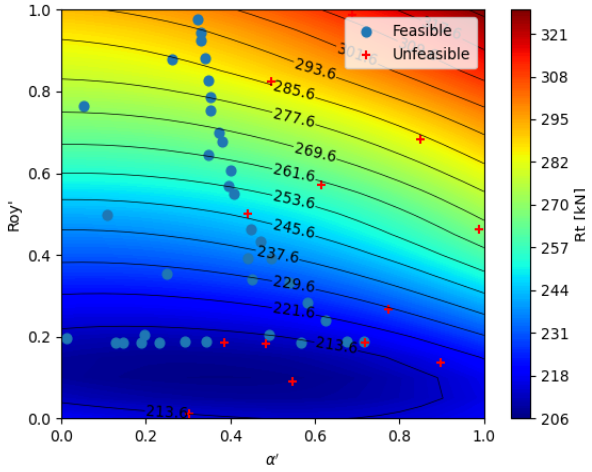

Figure 22: Mean prediction of R_t as a function of design parameters $(\alpha', R'_{oy}) \in \Omega'$

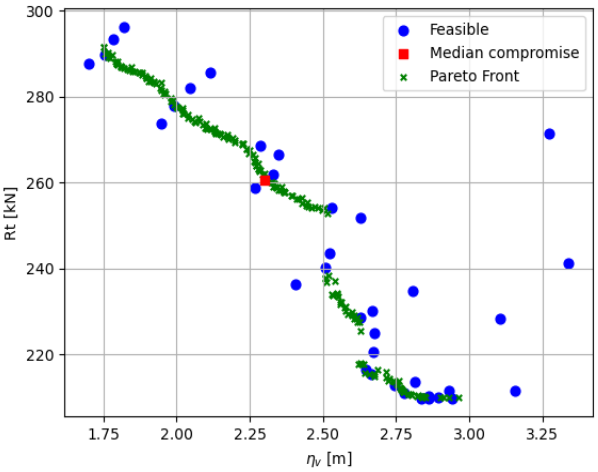

Figure 23: Objective functions values of the Pareto Front, median compromise and feasible designs - Medium fidelity level

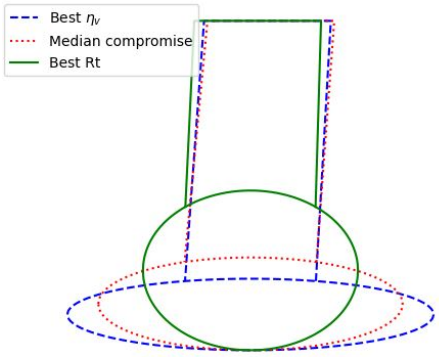

Figure 24: Cross-sectional diagram of the geometries with the best η_v, the median compromise and the best R_t - Median fidelity level

Characteristic	Value
(α', R'_{oy})	(0.39, 0.62)
η_v	2.30 m
R_t	261 kN

Table 5: Characteristic of the median compromise - Medium fidelity level

It can been noted from Figure 22 that the resistance of the ship is primarily affected by the torpedo's radius. In order to explain this effect, two geometries with opposite radius and having similar angle of strut inclination were extracted from the optimization process: the geometries of iterations 25 and 45. Their characteristics are given in Table 6.

Geometry	(α', R'_{oy})
25	(0.33, 0.98)
45	(0.34, 0.19)

Table 6: Dimensionless parameters of the geometries 25 & 45

The comparison of the hydrodynamic pressure coefficient distribution along the hull for these two geometries is also presented in Figure 25. It can be seen that there are major differences in the pressure distribution between the two designs. These differences affect the hydrodynamic forces and moments applied to the hull. The resistance

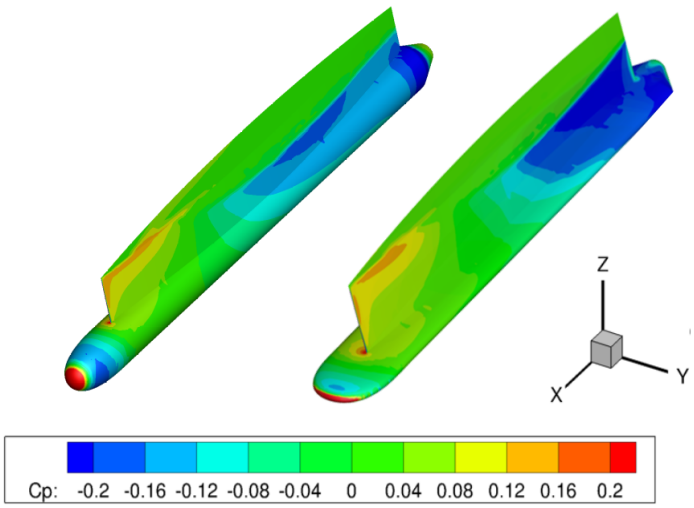

Figure 25: Comparison of the hydrodynamic pressure distribution of the geometry 45 (left) & 25 (right)

components (wave resistance R_w and viscous resistance R_v) of the strut and the torpedo have been extracted from RANS computations and are detailed in Table 7. The wave resistance of both torpedoes appears to be similar in the present comparison. However, it can been noted from the Table 7 that the increase in the total ship resistance of the geometry 25 is caused by the strut. This is explained by the fact that this one is deeper and has a much larger wetted area, resulting in increased hydrodynamic resistance.

	Strut		Torpedo	
Geometry	R_w	R_v	R_w	R_v
25	109	29	100	51
45	53	17	96	45

Table 7: Comparison of the different components of the ship resistance (in kN)

6.3. High fidelity level: Total ship resistance - free sinkage, fixed trim & fins

On the third degree of fidelity, the drag of the stabilizing fins is added to the total ship resistance. Their angle of attack varies in such a way to ensure that their lift balances the hydrodynamic pitching moment. Thus, the trim remains at zero, avoiding increasing the mesh deformation and consequently computational costs.

The convergence of the optimization loop is studied by assessing the location of the median compromise, its objective functions values as well as the IGD (see Figures 26-27).

The design parameters of the median compromise converge in the same range (α', R'_{oy}) $\approx$ (0.4,0.6), as well as η_v $\approx$ 2.3 m (see Figure 26). As shown in Figure 27, the IGD tends to zero, confirming the convergence.

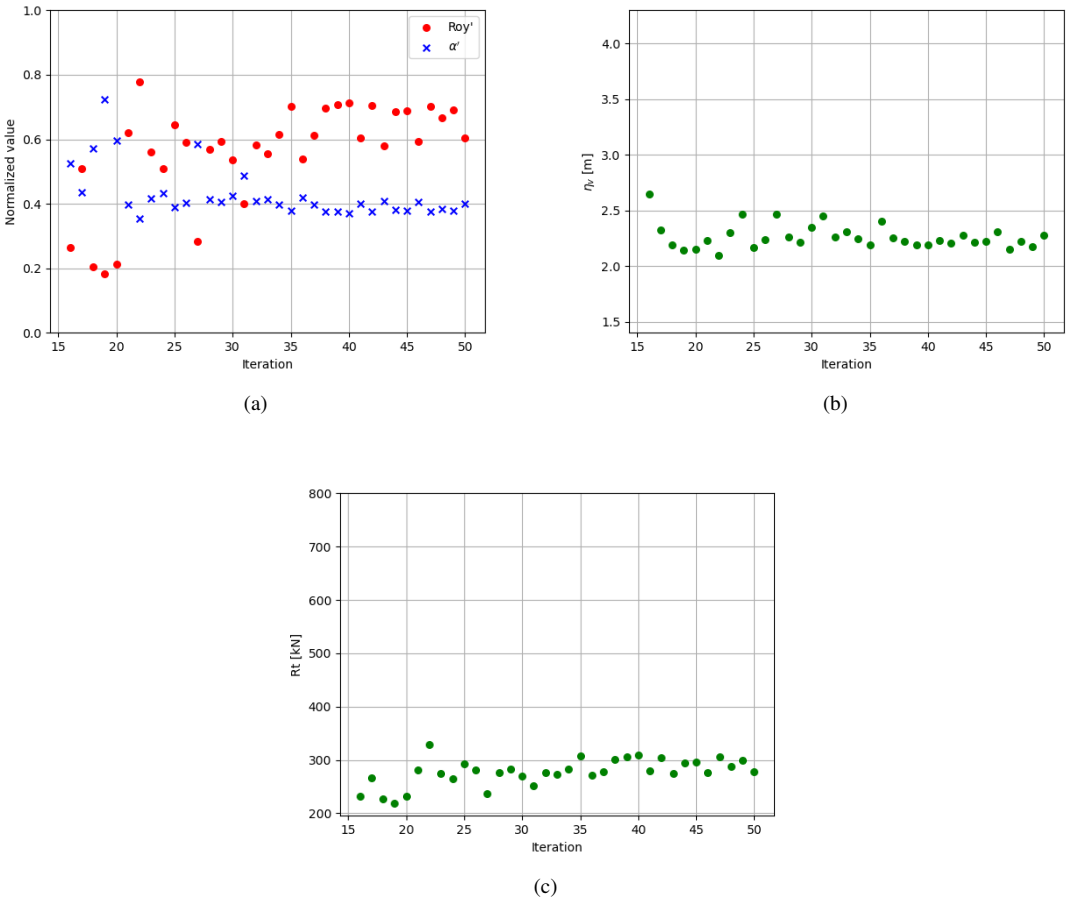

Figure 26: Iterative variation of design parameters α'and R'_{oy} (a) and objective functions values of the median compromise η_v (b) and R_t (c) - High fidelity level

Results at the last iteration, of the high fidelity problem solving, are presented in Figures 28-31. The trend of R_t with and without fins are similar. R_t is increasing by moving to the top right on the variability domain (see Figures 22 and 28), where values sharply increase with fins on the top right corner of the variability domain, and approximately 10% higher on the median compromise location.

Disregarding fins on SWATH resistance can lead to inaccurate results and incorrect sizing of the propulsion. A GP model of the fins angle response to reach ship trim equilibrium is built and given in Figure 29. The evolution of the fins angle is directly linked to the speed limit for stability (see Figure 8). The lower the speed limit, the higher the fins activity, and hence the drag. As the fins geometry is fixed, they are not suitable for all hulls. For instance, on the top right corner, the fins are obviously undersized. Fin angles of more 50° are found (see Figure 29). Stall may occur at great angles of attack and then drag is significantly increased. For geometries located on the Pareto Front, fins angles are ranged between 0° and 25° which. Some geometries do not need fins activity as AoA remains at 0°, meaning that the speed limit should be over 20 kt. Thus, there is a slight difference between the true speed limit and its prediction (see Figure 8, given that simplifications and approximations are used (see Section 4.3), and the fins still

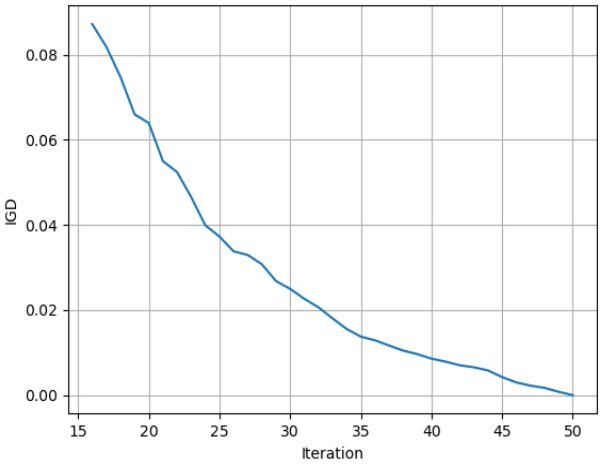

Figure 27: Iterative variation of the Inverted Generational Distance - High fidelity level

generate some lift.

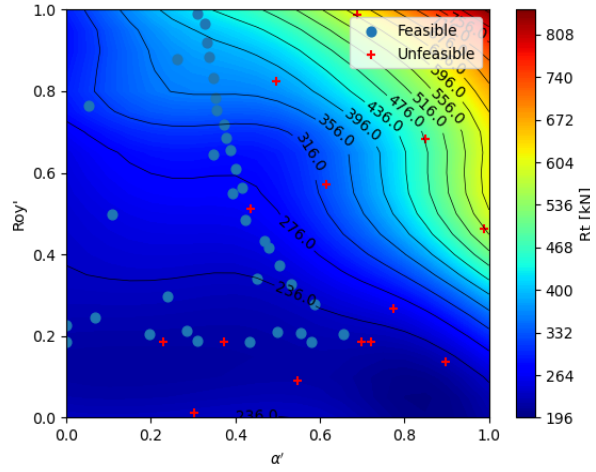

Figure 28: Mean prediction of R_t as a function of design parameters $(\alpha', R'_{oy}) \in \Omega'$

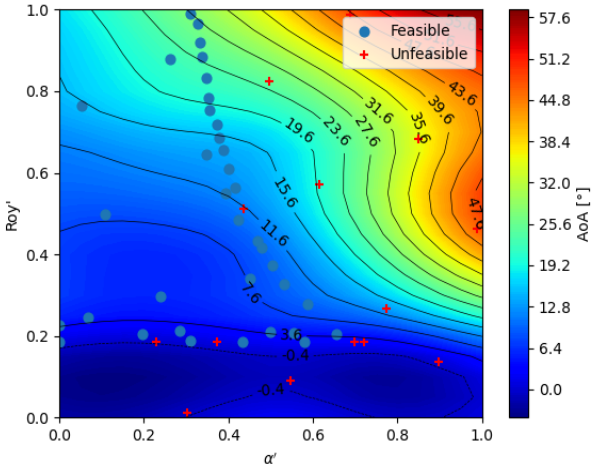

Figure 29: Mean Prediction of AoA as a function of design parameters $(\alpha', R'_{oy}) \in \Omega'$

The PF remains discontinuous (see Figures 30-31), but the median compromise remains in the same range (α', R'_{oy}) ≈ (0.4,0.6) (see Figure 26). The geometries minimizing R_t, η_v and the median compromise are similar to the previous cases (see Figures 19 and 24). Between two opposite optima, R_t and η_v can be respectively decreased by nearly 50% and 40%. The median compromise is listed in Table 8.

Characteristic	Value
(α', R'_{oy})	(0.40, 0.61)
η_v	2.27 m
R_t	278 kN

Table 8: Characteristic of the median compromise - High fidelity level

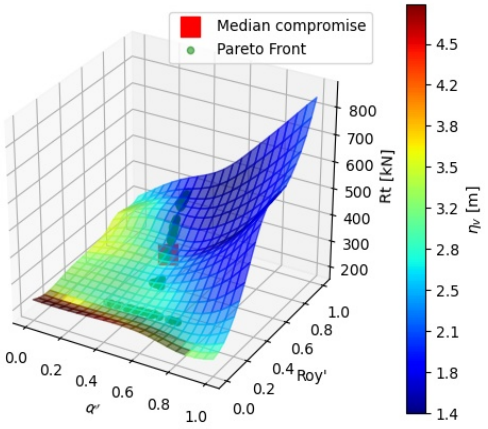

Figure 30: Mean prediction of the objective functions, Pareto Front and median compromise as a function of design parameters $(\alpha', R'_{oy}) \in \Omega'$ with R_t in vertical axis and η_v in color - High fidelity level

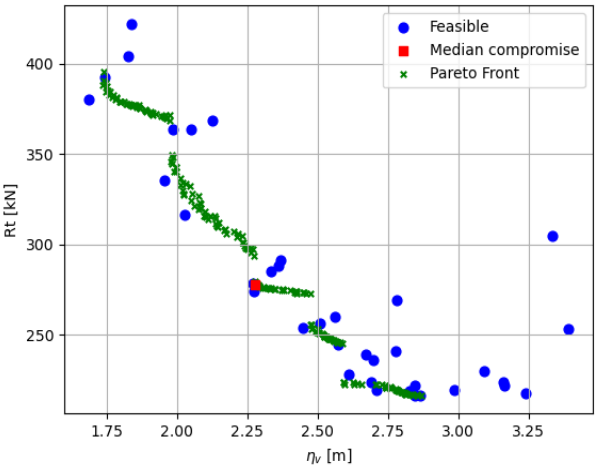

Figure 31: Objective functions values of the Pareto Front, median compromise and feasible designs - High fidelity level

The locations of the median compromise are very similar regardless of the three degrees of fidelity. This is confirmed by Figure 32, whereby the median compromise geometries sections of the three fidelity levels do not present any significant differences.

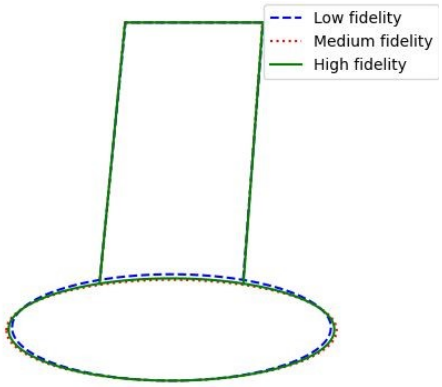

Figure 32: Cross-sectional diagram of the median compromises for the three fidelity levels

The relative differences of the location of the median compromises compared to the third fidelity level are given in Table 9. It is clearly demonstrated that both median compromises of low and medium-fidelity levels are very close

to the highest level of fidelity. It means that the median compromise is captured well by the low-fidelity levels, and so both models are usable.

Characteristic	Low	Medium	High
(α', R'_{oy})	(0.41, 0.57)	(0.39, 0.62)	(0.40, 0.61)
Relative difference	(2,0%, -1.2%)	(-2.1%, 1.3%)	-

Table 9: Location comparisons of the first two fidelity levels median compromises computed at the high-fidelity level

CPU time of each optimization must be considered: approximately 10, 30, and 120 minutes are required per iteration respectively for the first, second, and third fidelity levels. It is therefore important to quantify the expected accuracy with respect to the resources that it is necessary to obtain the results.

7. Conclusion

In the present study, a multi-objective SWATH hull form optimization using Gaussian process surrogate models is implemented to find the median compromise between seakeeping performance and ship resistance. The goal is to propose an efficient method for the design of SWATH ships considering particularities of this type of ship (such as viscous effects in seakeeping prediction and longitudinal stability for resistance calculation) and assessing the three degrees of fidelity for the ship resistance.

The studied ship is a 50m SWATH ship sailing in a wind turbine farm to transport technicians to and from offshore platforms. The significant amplitude of the vertical motion is evaluated in irregular waves. Viscous and fin effects are added to the results of a linear potential code in the equations of motion. The method is validated with experimental data. As the seakeeping model is not valid for certain geometries, a constraint on the semi-axis of the torpedoes is implemented. Also, a minimum longitudinal metacentric height constraint is imposed to reflect what a naval architect might face, including regulations. The ship displacement remains constant and is balanced by the vertical semi-axis of the torpedoes. The first level of fidelity for the ship resistance deals with the wetted surface. Then, the resistance is calculated using RANS simulations. SWATH ships being dynamically unstable at high speed, the longitudinal stability is assessed, what to the authors' knowledge has not been conducted in previous studies. In the present paper, all geometries are dynamically unstable in pitch and heave. Consequently, simulations are performed with free sinkage and fixed trim without fins. Finally, in a third level of fidelity, fins are added to the geometry to balance the Munk moment. Fins drag is then considered.

Gaussian processes and the "Minimization of the Variance of the Predicted Front" algorithm are used to populate the metamodel database. The final design is elected according to a new proposed criterion, the "Median Compromise of the Pareto Front".

The first case, considering the wetted surface, shows that seakeeping performance and wetted surface are indeed opposite functions. Geometries which minimize vertical amplitude of motion have a large horizontal semi-axis and large strut inclination angle, but those parameters increase the wetted surface. The use of a multi-objective algorithm to find the best compromise is then justified. The second case aims to study the ship resistance without fins. As all geometries are unstable, only sinkage is free. This study highlights that the resistance and the wetted surface evolve similarly, particularly for deep immersed hulls. Consequently, wetted surface could be a good indicator in term of bare hull resistance for a SWATH hull shape. Finally, the third case deals with stabilizing fins. Aft and forward fins are incorporated to the geometry. Their angle of attack is solved to balance the hydrodynamic moment. Geometries with a low speed limit for stability need more fin activity, leading to an increase of the total ship resistance.

The median compromises of the three cases are similar and located in the same range of the variability domain (α', R'_{oy}) $\approx$ (0.4, 0.6). The difference in location between the three median compromises is of the order of 2%. However, the calculation time for the third step is significantly greater than for the other two. From an industrial point of view, it would therefore be judicious to use the first or the second fidelity level to determine the median compromise.

In future work, non-linearity in the seakeeping model could be implemented, increasing the accuracy of the calculation of ship motion in irregular waves.

Furthermore, several infilling criteria, such as SUR (Picheny, 2015), EHVI (Emmerich et al., 2011), EI (Passos and Luersen, 2018), etc., can be compared in terms of convergence speed of the median compromise. Finally, a multi-fidelity surrogate-based approach (Sacher et al., 2021) may also be promising for solving this multi-objective SWATH hull form optimization problem.

Declaration of competing interest

The authors declare that they have no known competing financial interests or personal relationships that could have appeared to influence the work reported in this paper.

Acknowledgments

The work presented in this article is funded by ADEME as part of the *WindKeeper* project. This project is supported by the CNIM and consists of developing an innovative vessel dedicated to the maintenance of offshore wind turbines. The members of the consortium are the shipping company Chambon, Socarenam, Bertin Technologies, SeaTech Toulon, SUPMECA and ENSTA Bretagne.

Sample CRediT author statement

Paul Renaud: Methodology, Software, Writing - Original Draft, Writing - Review & Editing **Matthieu Sacher**: Methodology, Software, Writing - Original Draft, Supervision, Writing - Review & Editing **Yves-Marie Scolan**: Writing - Review & Editing, Project administration

References

S. Cordier, L. Morand, J.-M. Roux, Application of openfoam® to hull form optimisation at stx france, in: International Conference on Developments in Marine CFD 2011, London, United Kingdom, 2011.

A. Serani, G. Fasano, G. Liuzzi, S. Luicidi, U. Iemma, E. F. Campana, F. Stern, M. Diez, Ship hydrodynamic optimization by local hybridization of deterministic derivative-free global algorithms, Applied Ocean Research 59 (2016) 115–128.

Y. Tahara, D. Peri, E. F. Campana, F. Stern, Single- and multiobjective design optimization of a fast multihull ship: numerical and experimental results, Journal of Marine Science and Technology 16 (2011) 412–433.

M. Diez, A. Serani, E. F. Campana, O. Goren, K. Sarioz, D. B. Danisman, G. Grigoropoulos, E. Aloniati, M. Visonneau, P. Queutey, F. Stern, Multi-objective hydrodynamic optimization of the dtmb 5415 for resistance and seakeeping, in: 13th International Conference on Fast Sea Transportation - FAST 2015, Washington DC, United States., 2015.

L. Yun, A. Bliault, H. Zong Rong, High Speed Catamarans and Multihulls, Springer, 2019.

C. Lee, M. Martin, Determination of Size of Stabilizing Fins for Small Waterplane Area Twin-Hull Ships, Technical Report, David Taylor Naval Ship Research And Development, 1976.

Y. Lin, Q. Yang, G. Guan, Automatic design optimization of swath applying cfd and rsm model, Ocean Engineering 172 (2019) 146–154.

Q. Ni, W. Ruan, S. Li, F. Zhao, Multiple speed integrated optimization design for a swath using sbd technique, The Journal of Marine Science and Technology 25 (2020) 185–195.

C. Papandreou, A. Papanikolaou, Parametric design and multi-objective optimization of swath, in: 5th International Symposium on Ship Operations, Management and Economics, Athens, 2015.

R. Pellegrini, A. Serani, S. Harries, M. Diez, Multi-objective hull-form optimization of a swath configuration via design-space dimensionality reduction, multi-fidelity metamodels, and swarm intelligence, in: 7th International Conference on Computational Methods in Marine Engineering, Nantes, France, 2017, pp. 95–106.

E. Begovic, C. Bertorello, S. Mancini, Hydrodynamic performances of small size swath craft, Brodogradnja/Shipbilding 66 (2015) 1 – 22.

G. Guan, Q. Yang, Y. Wang, S. Zhou, Z. Zhuang, Parametric design and optimization of swath for reduced resistance based on evolutionary algorithm, Journal of Marine Science and Technology 26 (2020) 54–70.

L. Bonfiglio, P. Perdikaris, G. Vernengo, J. Seixas de Medeiros, G. Karniadakis, Improving swath seakeeping performance using multi-fidelity gaussian process and bayesian optimization, Journal of Ship Research 62 (2018) 223 – 240.

L. Bonfiglio, S. Brizzolara, C. Chrissostomidis, Viscous free surface numerical simulations of oscillating swath ship sections, Recent Researches in Mechanical Engineering (2013) 33–38.

J. Wackers, C. Jeanson, P. Queutey, M. Visonneau, R. Pellegrini, A. Serani, M. Diez, Hull shape optimisation using multi-fidelity metamodels and adaptive grid refinement, in: 13th International Conference on Fast Sea Transportation - FAST 2015, Washington DC,st Numerical Towing Tank Symposium (NuTTs 2018), Cortone, Italy, 2018.

G. Matheron, Principles of statistics, Economic geology 58 (1963) 1246–1266.

J. Guerrero, A. Cominetti, J. Pralits, D. Villa, Surrogate-based optimization using an open-source framework: The bulbous bow shape optimization case, Mathematical and Computational Applications 23 (2018).

A. G. d. Passos, M. A. Luersen, Multi-objective optimization with kriging surrogates using "moko", an open source package, Latin American Journal of Solids and Structures 15 (2018).
S. Brizzolara, Parametric optimization of swat-hull forms by a viscous-inviscid free surface method driven by a differential evolution algorithm, in: 25th Symposium on Naval Hydrodynamics, St. John's, Newfoundland and Labrador, Canada, 2004.
R. Latorre, J. Vasconsellos, Study of hull angle influence on swath heave and pitch motions, Naval Engineers Journal 113 (2008) 63–70.
X. Chen, Hydrodynamics in offshore and naval applications, The IES Journal Part : Civil & Structural Engineering 4 (2011) 124–142.
X. Sun, C. Yao, Q. Ye, Numerical investigation on seakeeping performance of swath with three dimensional translating-pulsating source green function, Engineering Analysis with Boundary Elements 73 (2016) 215–225.
C. Lee, Theoretical prediction of motion of small waterplane area, twin-hull (SWATH) ships in waves, Technical Report, David Taylor Naval Ship Research And Development, 1976.
S. Huston, Structural health monitoring of a high-speed naval vessel using ambient vibrations, Master's thesis, Georgia Institute of Technology, 2021.
IEC, IEC 61400-3 Wind turbines Part 3: Design requirements for offshore wind turbines, Technical Report, 2009.
B. Abeil, Windkeeper wind farm support vessel (46.0 m); zero speed model tests, 2017. Personal communication.
P. Queutey, M. Visonneau, An interface capturing method for free-surface hydrodynamic flows, Computers & Fluids 36 (2007) 1481–1510.
O. M. Faltinsen, Sea Loads on Ships and Offshore Structures, Cambridge University Press, 1990.
P. Hooijmans, Swath (windkeeper project); longitudinal stability assessment, 2016. Personal communication.
N. Bigi, Stabilité longitudinale des navires de type small waterplane area twin hull: Swath, 2018. Personal communication.
D. G. Krieg, A statistical approach to some basic mine valuation problems on the witwatersrand, European Journal of Operational Research 52 (1951) 119–139.
M. D. Mckay, R. Beckman, W. Conover, A comparison of three methods for selecting vales of input variables in the analysis of output from a computer code, Technometrics 21 (1979) 239–245.
C. M. Fonseca, P. J. Fleming, Multiobjective optimization and multiple constraint handling with evolutionary algorithms. i. a unified formulation, IEEE Transactions on Systems, Man, and Cybernetics-Part A: Systems and Humans 28 (1998) 26–37.
K. Deb, A. Pratap, S. Agarwal, T. Meyarivan, A fast and elitist multiobjective genetic algorithm: Nsga-ii, IEEE transactions on evolutionary computation 6 (2002) 182–197.
C. A. C. Coello, G. B. Lamont, D. A. Van Veldhuizen, et al., Evolutionary algorithms for solving multi-objective problems, volume 5, Springer, 2007.
R. Huang, X. Luo, B. Ji, P. Wang, A. Yu, Z. Zhai, J. Zhou, Multi-objective optimization of a mixed-flow pump impeller using modified nsga-ii algorithm, Science China technological sciences 58 (2015) 2122–2130.
H. Lim, H. Kim, Multi-objective airfoil shape optimization using an adaptive hybrid evolutionary algorithm, Aerospace Science and Technology 87 (2019) 141–153.
T. Simpson, J. Poplinski, N. P. Koch, J. Allen, Metamodels for computer-based engineering design: Survey and recommendations, Engineering with Computers 17 (2001) 129–150.
C. E. Rasmussen, C. K. I. Williams, Gaussian Processes for Machine Learning, MIT Press, 2006.
J. P. Kleijnen, Kriging metamodeling in simulation: A review, European Journal of Operational Research 192 (2009) 707 – 716.
V. Picheny, T. Wagner, D. Ginsbourger, A benchmark of kriging-based infill criteria for noisy optimization, Structural and Multidisciplinary Optimization 48 (2013) 607–626.
D. R. Jones, M. Schonlau, W. J. Welch, Efficient Global Optimization of Expensive Black-Box Functions, Journal of Global optimization 13 (1998) 455–492.
M. Sacher, F. Hauville, R. Duvigneau, O. Le Maître, N. Aubin, M. Durand, Efficient optimization procedure in non-linear fluid-structure interaction problem: Application to mainsail trimming in upwind conditions, Journal of Fluids and Structures 69 (2017) 209 – 231.
M. Sacher, M. Durand, E. Berrini, F. Hauville, R. Duvigneau, O. Le Maître, J.-A. Astolfi, Flexible hydrofoil optimization for the 35th america's cup with constrained ego method, Ocean Engineering 157 (2018) 62–72.
M. Meliani, N. Bartoli, T. Lefebvre, M.-A. Bouhlel, J. Martins, J. Morlier, Multi-fidelity efficient global optimization : Methodology and application to airfoil shape design, in: AIAA Aviation 2019 Forum,Dallas, United States, 2019.
T. Wagner, M. Emmerich, A. Deutz, W. Ponweiser, On expected-improvement criteria for model-based multi-objective optimization, in: International Conference on Parallel Problem Solving from Nature, Springer, 2010, pp. 718–727.
J. D. Svenson, T. J. Santner, Multiobjective optimization of expensive black-box functions via expected maximin improvement, The Ohio State University, Columbus, Ohio 32 (2010).
A. J. Keane, Statistical improvement criteria for use in multiobjective design optimization, AIAA journal 44 (2006) 879–891.
M. T. Emmerich, K. C. Giannakoglou, B. Naujoks, Single-and multiobjective evolutionary optimization assisted by gaussian random field metamodels, IEEE Transactions on Evolutionary Computation 10 (2006) 421–439.
M. T. Emmerich, A. H. Deutz, J. W. Klinkenberg, Hypervolume-based expected improvement: Monotonicity properties and exact computation, in: 2011 IEEE Congress of Evolutionary Computation (CEC), IEEE, 2011, pp. 2147–2154.
C. Luo, K. Shimoyama, S. Obayashi, Kriging model based many-objective optimization with efficient calculation of expected hypervolume improvement, in: 2014 IEEE Congress on Evolutionary Computation (CEC), IEEE, 2014, pp. 1187–1194.
V. Picheny, Multiobjective optimization using gaussian process emulators via stepwise uncertainty reduction, Statistics and Computing 25 (2015) 1265–1280.
M. Binois, D. Ginsbourger, O. Roustant, Quantifying uncertainty on pareto fronts with gaussian process conditional simulations, European journal of operational research 243 (2015) 386–394.
A. G. d. Passos, M. A. Luersen, Multiobjective optimization of laminated composite parts with curvilinear fibers using kriging-based approaches, Structural and Multidisciplinary Optimization 57 (2018) 1115–1127.
K. Shimoyama, S. Jeong, S. Obayashi, Kriging-surrogate-based optimization considering expected hypervolume improvement in non-constrained many-objective test problems, in: 2013 IEEE Congress on Evolutionary Computation, IEEE, 2013, pp. 658–665.

M. Sacher, O. Le Maître, R. Duvigneau, F. Hauville, M. Durand, C. Lothodé, A non-nested infilling strategy for multifidelity based efficient global optimization, International Journal for Uncertainty Quantification 11 (2021) 1–30.